Understanding the synergistic mechanism of single atom Co-modified perovskite oxide for piezo-photocatalytic CO_2 reduction

Qijun Xu, Lilian Wang, Xuelin Sheng, Yongxin Yang, Conghui Zhang, Lingyan Duan, Hong Guo [*],[1]

International Joint Research Center for Advanced Energy Materials of Yunnan Province, Yunnan Key Laboratory of Carbon Neutrality and Green Low-carbon Technologies, School of Materials and Energy, Yunnan University, Kunming 650091, China

ARTICLE INFO

ABSTRACT

The synergistic effect of novel piezoelectric catalysis and traditional photocatalysis can significantly enhance catalytic performance. Herein, we design novel heterojunction piezo-photocatalysts combining Co-N-C and $BiFeO_3$ (BFO), the yields of CO_2 reduction to CO and CH_4 with Co-N-C@BFO(1:7) catalyst are up to 1373.41 μmol/g and 169.32 μmol/g, respectively. The displacement current, energy band theory, piezoelectric effect, and in-situ DRIFTS are combined to explain the mechanism. In piezo-photocatalysis, displacement current generates time-varying electrostatic potential, which transfers electrons to the Co-N-C active site and promotes CO_2RR. The energy band of the BFO supplier meeting the potential requirements also promotes electron transfer to the Co-N-C active site to participate in CO_2RR. The combination of piezoelectric electric fields and visible lights promotes charge separation and improves catalytic activity. This work provides a profound understanding and a new idea for piezo-photocatalytic reduction of CO_2.

1. Introduction

In recent years, CO_2 has brought serious environmental crises to the world [1–3]. Therefore, converting CO_2 into renewable fuels has become the focus of research [4,5]. However, due to the limited energy of photocatalysis, the reduction efficiency is low. Hence, the research on CO_2RR still poses great challenges [6,7]. Notably, piezoelectric catalysis can produce piezoelectric polarization by coupling ferroelectric materials (Scheme 1). The piezoelectric field generated by piezoelectric polarization largely inhibits the recombination of carriers, thereby improving the performance of CO_2RR [8,9]. Obviously, piezo-photocatalysis can greatly promote the CO_2RR reaction.

Mechanical vibration will cause the catalyst to deform under stress, thus generating a displacement current which can spontaneously participate in the reaction [10–13]. The displacement current will form a static electric potential on the catalyst and change over time [14–17]. The micro-bubbles generated during mechanical vibration can provide pressure to time-varying for catalysts to achieve piezoelectric catalysis [18–22]. Consequently, the generation of time-varying electrostatic potential and displacement current is unstable [23–25]. Meanwhile,

only by meeting the requirements of band structure of the catalyst can the required catalytic reaction be carried out [26–28]. Mechanical vibration can cause changes in the band structure of the catalyst, promoting the progress of CO_2RR reaction. Therefore, during the ultrasonic vibration of the catalyst, the alteration in the band structure and the formation of displacement current greatly improve the performance of CO_2RR [29–32].

Usually, the crystal structure affects its piezoelectric properties. BFO is chosen as a piezoelectric supplier because of its cubic unit structure at room temperature and exceptional piezoelectric response [33]. Bi^{2+} is situated at the cube's eight corners, while the O^{2-} ion is centered on the cube's six surfaces, and the Fe^{4+} ion is located above (or below) the cube's center [34]. According to the asymmetric characteristics of the BFO crystal structure, the centers of negative and positive ions do not coincide [35]. Therefore, there is an electric dipole moment on the z-axis in the BFO, and the BFO has the property of autonomous polarization [36]. When stress squeezes the BFO, the z-axis tensile deformation causes the Fe^{4+} ion to shift along the z-axis, which changes the electric dipole moment, produces polarization, and stockpiles a large amount of charge on the surface of the BFO [37]. However, a large amount of

---

charge accumulation can inhibit CO_2RR to some extent. Hence, it is necessary to separate the charge accumulated on the BFO surface and transfer the electrons to a highly active catalyst surface for CO_2 reduction. Interestingly, the Co-N-C catalyst has excellent catalytic activity, CO-selectivity, and low cost. More importantly, it has a rich CO_2RR reaction active site, which is an excellent choice [38]. Therefore, the Co-N_x portion is considered to be the most effective active site for CO_2RR [39, 40].

According to the principle of displacement current, piezoelectric catalysis makes BFO produce displacement current and generate electrostatic potential varying with time [41,42]. The electrostatic potential with time-varying drives the piezoelectric effect to generate an electron flow, which then transfers through the BFO surface to the Co-N-C surface. In addition, the Co-N-C@BFO catalyst produces more photogenerated electron-hole pairs under light conditions. The displacement current generated by these electron-hole pairs through the piezoelectric effect promotes electron-hole separation, thus allowing more electrons to migrate to the active site Co-N-C to partake in the CO_2 catalytic reduction. Thus, piezo-photocatalysis can increase the ability of CO_2 catalytic reduction. However, the current explanation of the mechanisms related to the reduction of CO_2 by piezo-photocatalysis is not clear enough, resulting in obstacles for readers in their understanding process.

Herein, we synthesized the Co-N-C@BFO catalyst and its properties of photocatalysis, piezoelectric catalysis, and piezo-photocatalysis for CO_2 reduction were tested. We find that the Co-N-C@BFO catalyst has excellent CO_2RR behavior under the conditions of piezo-photocatalysis. The piezoelectric properties of the catalyst are validated via using PFM analysis and analyzed the mechanisation of piezo-photocatalytic CO_2 reduction. To probe the path and intermediate products of CO_2 reduction, we conduct in-situ DRIFTS test analysis. This study can provide useful guidance for the design of efficient piezo-photocatalysts for CO_2 reduction, and provide a reference for further research on the mechanism of piezo-photocatalytic CO_2 reduction.

2. Experimental section

This part is presented in the Supporting Information.

3. Results and discussions

3.1. Structure and morphology

We have synthesized a BFO catalyst with high purity by the hydrothermal method. The preparation process flow for catalysts (Fig. 1a). X-ray diffraction (XRD) analysis was conducted on catalysts (Fig. S1). This confirms the crystal phases of each catalyst. We can easily see that the purity of the BFO catalyst is relatively high, which is the pure rhombohedral phase of BFO (JCPDS Card No. 86–1518). The XRD diffraction

peak of Co-N-C in Fig. S1a shows the peak of Co (JCPDS Card No. 15–0806) [43]. This not only confirmed the successful preparation of BFO and Co-N-C but also that the synthesized catalyst purity is high. The XRD of Co-N-C@BFO obtained by ball milling of Co-N-C and BFO shows no significant change (Fig. S1). This confirms the successful preparation of Co-N-C@BFO. Besides, we also conducted FT-IR analysis of catalysts, as can be seen in Fig. S2. The picture shows the infrared spectra of the catalysts in the range of 400–1600 cm^{-1}. We can clearly see that BFO and Co-N-C@BFO catalysts have strong absorption peaks near the wavelength of 532 cm^{-1}. This is due to the presence of a Fe_6 group in the perovskite structure of the BFO catalyst, and the absorption peak is formed by the bending and stretching of the Fe-O bond in the Fe_6 group [44]. It is easy to observe from the graph that both Co-N-C@BFO and BFO catalysts have absorption peaks, and the positions of the absorption peaks are basically the same, which again indicates the successful preparation of Co-N-C@BFO.

To observe the microscopic morphology of the catalysts, we conducted SEM on catalysts. The SEM pictures of Co-N-C@BFO, BFO and Co-N-C are shown in Fig. 1b-e. From the SEM graphics of the Co-N-C, it is easy to observe that the shape of the Co-N-C catalyst is uneven, similar to a globular structure, with a diameter of about 8 μm (Fig. 1b). The morphology of the BFO catalyst is also irregular, and its size is also inconsistent (Fig. 1c-d). The BFO catalyst without grinding is agglomerated, forming larger BFO catalyst particles. The shape of Co-N-C@BFO obtained by ball milling the Co-N-C and BFO catalysts is similar to that of a sphere, with a diameter of about 20 μm (Fig. 1e). Combining Fig. 1e with the EDS graphic of the Co-N-C@BFO, it can be seen that Co-N-C is uniformly distributed on the surface of BFO. To analyze the elemental distribution and content of the catalyst, we conducted EDS surface scanning, as shown in Figs. S3-S8. From the figure, it can be seen that the distribution of various elements in Co-N-C@BFO, BFO and Co-N-C catalysts is uniform. Combined with the element content in the catalyst, the successful synthesis of Co-N-C@BFO, BFO, and Co-N-C was again confirmed, and the results were in line with our XRD pattern analysis. So as to further analyze the microscopic morphology of the Co-N-C@BFO, we conducted TEM testing on it, as can be seen in Fig. 1f-p. The BFO phase has obvious lattice stripes, with lattice spacing of 0.29 and 0.34 nm (Fig. 1f-i). The tetragonal symmetry of the BFO phase in Co-N-C@BFO was confirmed by its crystal orientation. From the EDS element mapping of the Co-N-C@BFO, it is easy to observe that the O, N, Co, Bi, C, and Fe are uniformly spread in the Co-N-C@BFO. The above analysis indicates that Co-N-C@BFO was successfully prepared. We characterized the dispersed Co single atoms in Co-N-C@BFO catalyst using an aberration-corrected HAADF-STEM. The aberration-corrected HAADF-STEM image of Co-N-C@BFO catalyst is shown in Fig. 1q-r and Fig. S9. Many bright dots confirm that dispersed Co single atoms are loaded on Co-N-C@BFO catalyst and exhibit good dispersibility.
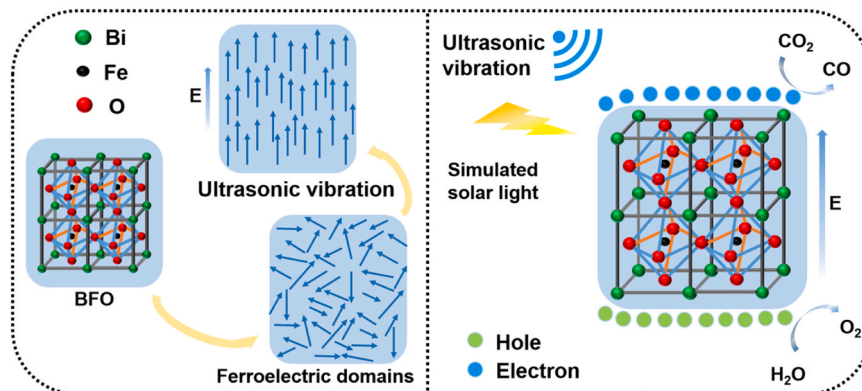
Scheme 1. Simplified mechanisation of piezo-photocatalytic CO_2RR.
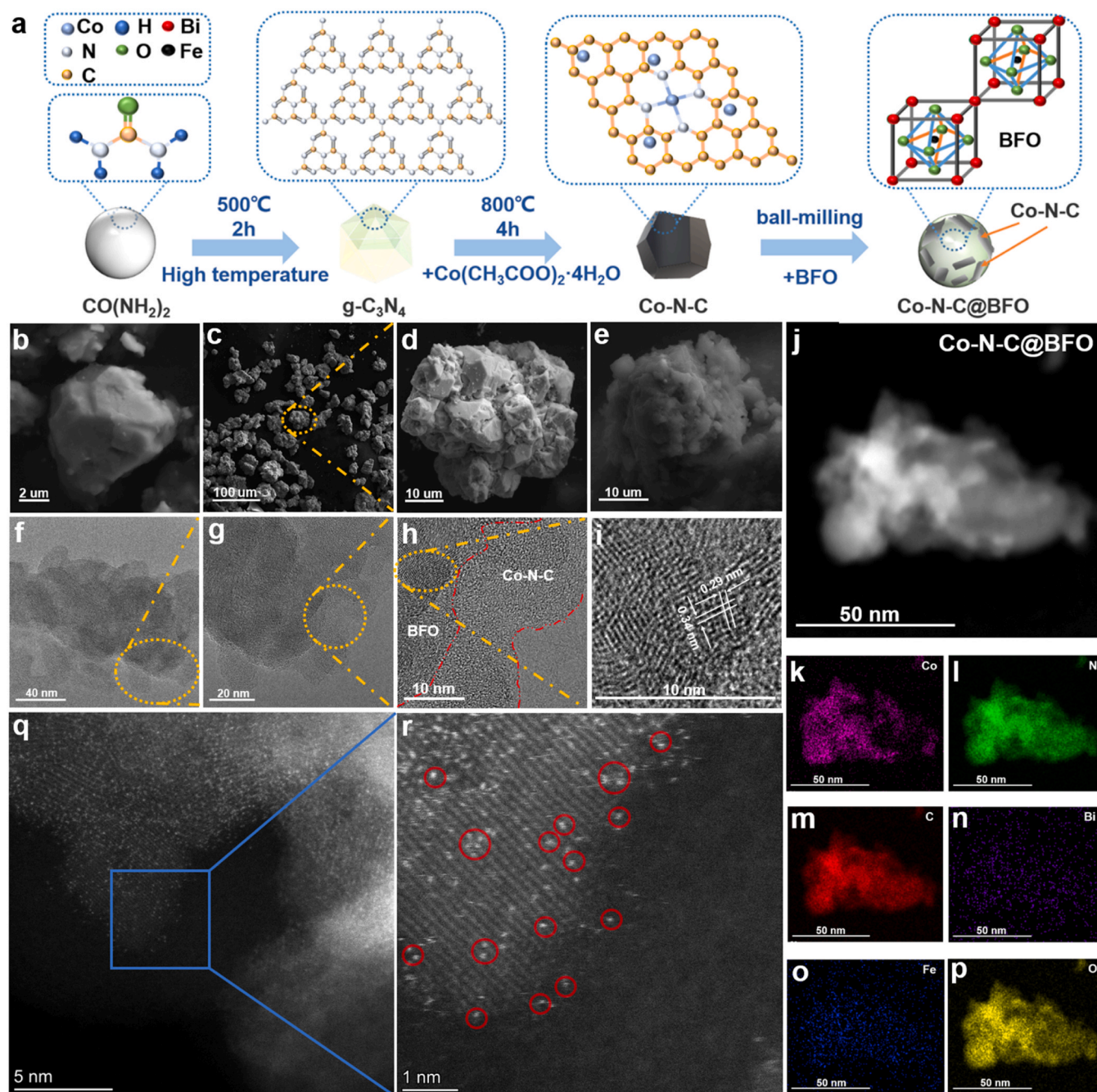
Fig. 1. (a) The synthesis process of Co-N-C@BFO samples. SEM graphic of (b) Co-N-C, (c)-(d) BFO, and (e) Co-N-C@BFO. (f)-(i) The HR-TEM picture of Co-N-C@BFO. (j)-(p) Elemental mappings of Co-N-C@BFO. (q)-(r) AC-HAADF-STEM picture of Co-N-C@BFO.

3.2. Identification of active site of catalyst

The total XPS spectra of catalysts can be seen in Fig. S10. There are Co 2p, C 1 s, and N 1 s of Co-N-C and O 1 s, Bi 4 f and Fe 2p of BFO in Co-N-C@BFO(1:7), which shows that the element peaks do not obviously change after the synthesis of Co-N-C@BFO(1:7). This indicates the successful preparation of the Co-N-C@BFO(1:7). The XPS of Co-N-C can be seen in Fig. 2a-c. Due to Co^{2+}, Co has two peaks at 779.9 and 795.7 eV, respectively, while the peaks of 783.4 and 801.45 eV are satellite peaks of Co^{2+} (Fig. 2a). The results show that the oxidation state of Co in Co-N-C is + 2. The peaks at 401.07, 400.56 and 398.6 eV are graphitic-N, pyrrolic-N and pyridinic-N (Fig. 2b). It can be seen that the amount of pyridinic-N dominates. This indicates that Co-N-C is normally prepared and becomes the active site of CO_2RR [45,46]. The peaks near

287.8, 285.63, and 284.2 eV are C=O, C-N, and C-C bonds, respectively (Fig. 2c). In addition, we also analyzed the XPS of the original BFO and Co-N-C@BFO(1:7). In the XPS spectrum of the original BFO, the peaks near 158.75 and 164.25 eV are Bi 4 $f_{7/2}$ and Bi 4 $f_{5/2}$ (Fig. 2d). The two peaks near 723.42 and 710.45 eV are Fe $2p_{1/2}$ and Fe $2p_{3/2}$, respectively. As shown in Fig. 2f, at 531.86 and 528.98 eV, the O 1 s peak has two parts, which are due to the bonded oxygen and lattice oxygen in the BFO crystal. Compared with the original BFO, the higher binding energy of the Bi 4 f, O 1 s, and Fe 2p peaks of Co-N-C@BFO(1:7) shifted slightly, and the shift value was about 0.6 eV. Therefore, Bi 4 $f_{5/2}$ and Bi 4 $f_{7/2}$ were transferred to the vicinity of 164.75 and 159.35 eV (Fig. 2d). Fe $2p_{1/2}$ and Fe $2p_{3/2}$ were transferred to the vicinity of 724.02 and 711.35 eV (Fig. 2e). Bonded O and lattice O transfer near 532.47 and 529.58 eV. The XPS spectrum in Fig. 2d-f shows that Co-N-C and BFO
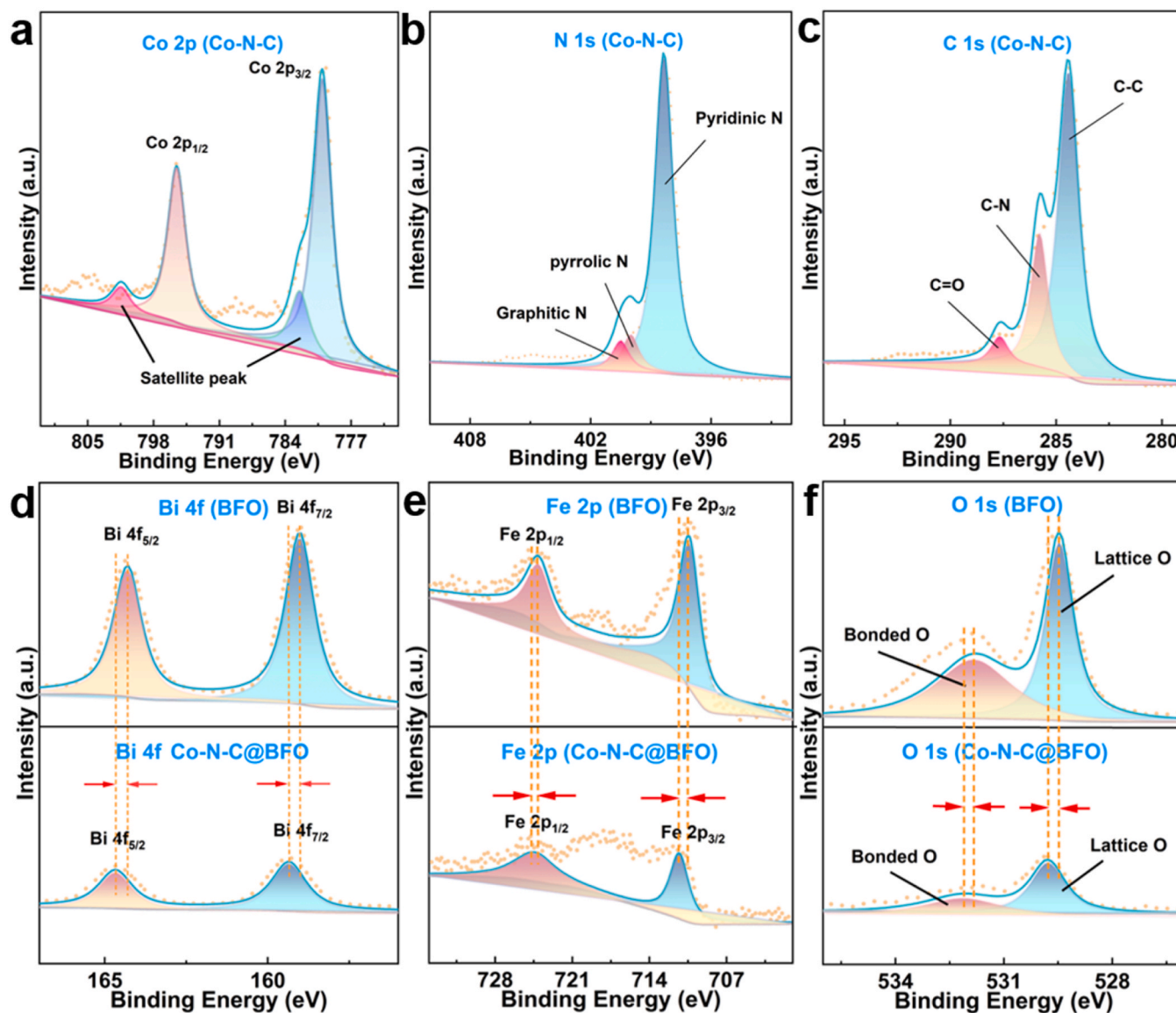
Fig. 2. The XPS spectra of (a) Co 2p (b) N 1 s (c) C 1 s (d)-(f) The contrast of the binding energy of Bi 4 f, O 1 s, and Fe 2p in Co-N-C@BFO(1:7) and BFO.

combine to form a strong binding force after ball milling. This also indicates that the prepared Co-N-C@BFO catalyst is stable to mechanical vibration.

3.3. Electrochemical characterization

We conducted corresponding electrochemical experiments to investigate the electrochemical performances of the catalysts [47]. First of all, the photoluminescence spectrum (PL) of the catalysts was tested (Fig. 3a). PL spectra can be used to measure the separating efficiency of the electric charge of catalysts. There is a similarity between the emission peaks of the BFO and the Co-N-C@BFO, which are both near 653 nm (Fig. 3a). The Co-N-C has a strong emission peak in the center. However, we can see by comparison that the peak intensity of the Co-N-C@BFO is the weakest, indicating that its photogenerated charge separation efficiency is the best. This is because the Co-N-C@BFO obtained by recombination accelerates the separation of photogenerated carriers so that electrons are transported to the active site of Co-N-C for the reduction reaction. The Co-N-C@BFO composite structure material synthesized by ball milling method has two phases: Co-N-C and BFO, and both phases have complete structures. There is a certain interaction

between the two, causing the emission peak of Co-N-C to red shift [48]. The photocurrent test results in Fig. 3c also indicate that the photoelectric performance of the Co-N-C@BFO is better. It has been proven that the separation efficiency of carriers has increased for the Co-N-C@BFO obtained after recombination. Fig. 3d shows the electrochemical impedance diagram (EIS) of catalysts. However, the Nyquist diagram for the Co-N-C@BFO shows a typical semicircle of reduced radius compared to pure BFO. This indicates that the mobility of charge carriers increases after BFO and Co-N-C recombination. The above electrochemical tests show that the photoelectric character of the Co-N-C@BFO is more conducive to the catalytic reaction and has higher catalytic activity.

The following is an in-depth analysis exploring the energy band structure. Perform VB-XPS detection on the catalysts, as can be seen in Fig. 3e. The VB potentials of Co-N-C@BFO, BFO, and Co-N-C were determined to be 2.18, 2.19 and 1.97 eV, respectively. Motshottky tests were performed on catalysts, and the Motshottky curves are shown in Fig. 3f. According to curve analysis, the flat band potentials of Co-N-C@BFO, BFO, and Co-N-C catalysts are 0.16, 0.12, and 0.41 eV, respectively. UV–vis DRS for catalysts as can be seen in Fig. 3g. It is easy to observe the comparison of light absorption of the catalyst in the same
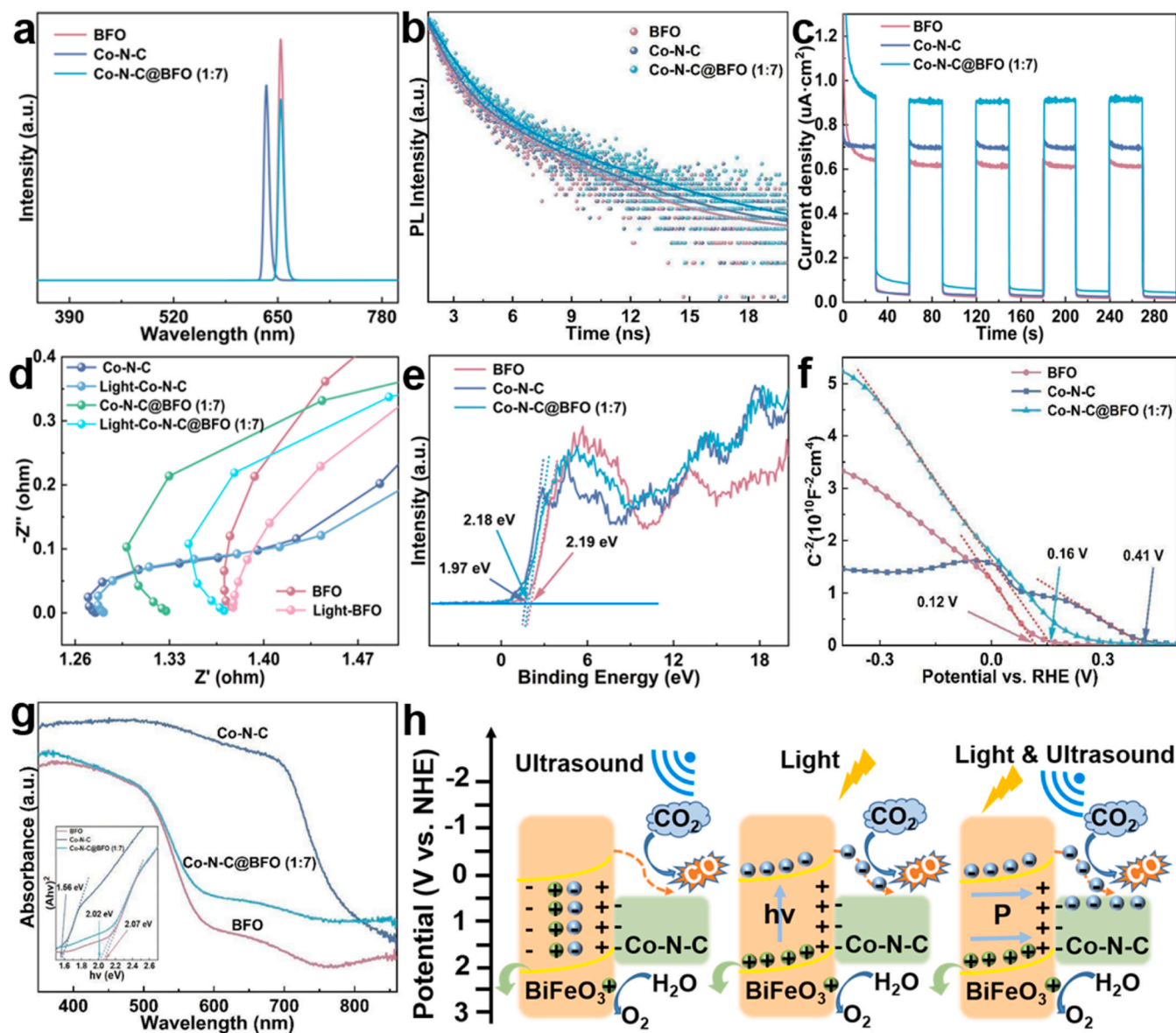
Fig. 3. (a) PL spectra of Co-N-C@BFO, BFO and Co-N-C (excitation wavelength is 325 nm). (b) Time-resolved PL decay spectra (c) Photocurrent (d) EIS Nyquist plots curves (e) Valence-band XPS spectra and (f) Motschottky curves of Co-N-C, BFO and Co-N-C@BFO. (g) UV–vis DRS of different catalyst samples. (h) The energy band structure of Co-N-C@BFO under different catalytic environments.

wavelength band. Based on comprehensive analysis, it can be concluded that the optical band gap values of Co-N-C@BFO, BFO and Co-N-C are 2.02, 2.07 and 1.56 eV, respectively.

We investigated the band structure of the Co-N-C@BFO catalyst under different catalytic environments (Fig. 3h). Ultrasonic vibration can generate a piezoelectric field within a material, directly stimulating electronic transitions. The energy band will be tilted by the piezoelectric field produced by piezoelectric polarization in piezoelectric catalysis. Thus, it is easier to meet the requirements of reduction potential and promote the catalytic reaction. In the Co-N-C@BFO, the holes will accumulate in VB, and the electrons will shift from VB to CB. Thus, the electrons are transferred to the active center on the surface of Co-N-C@BFO for CO_2 RR. It can be found that piezoelectric and photocatalytic processes can improve each other, which is consistent with our CO_2 reduction performance test results. In order to explore the fluorescence lifetime of catalysts, time-resolved PL decay spectra tests were conducted on catalysts, as can be seen in Fig. 3b. The Co-N-C@BFO has a longer fluorescence lifetime than Co-N-C and BFO catalysts because the separation efficiency of carriers in the Co-N-C@BFO is higher.

3.4. Piezoelectricity and piezocatalytic mechanism investigation

Piezoelectric response force microscopy (PFM) is a scanning probe technique that can measure piezoelectricity. To explore the piezoelectricity of catalysts, PFM trials were conducted on them, as can be seen from Fig. S11 and Fig. 4. The morphologies, vertical piezoelectric response amplitudes, and phase images of Co-N-C@BFO are shown in Fig. 4a-f. From the graph, it can be clearly observed that the morphologies, phase, and amplitude of the Co-N-C@BFO catalyst change under the applied induced voltage. This can be explained by the piezoelectric response generated by the Co-N-C@BFO, which results in its piezoelectricity. The local polarization of the catalyst was demonstrated by PFM. The typical amplitude voltage butterfly curve of $-10 \sim +10$ V is obtained through testing, as shown in Fig. 4g. A phase transition of ≈ 80 exists in the voltage lag loop of the Co-N-C@BFO (Fig. 4h). The phase angle undergoes an 80° change. It fully verifies the piezoelectricity of the catalyst and offers a clear basis.

In this work, the piezoelectric catalytic mechanism is studied by combining displacement current, energy band theory, and the
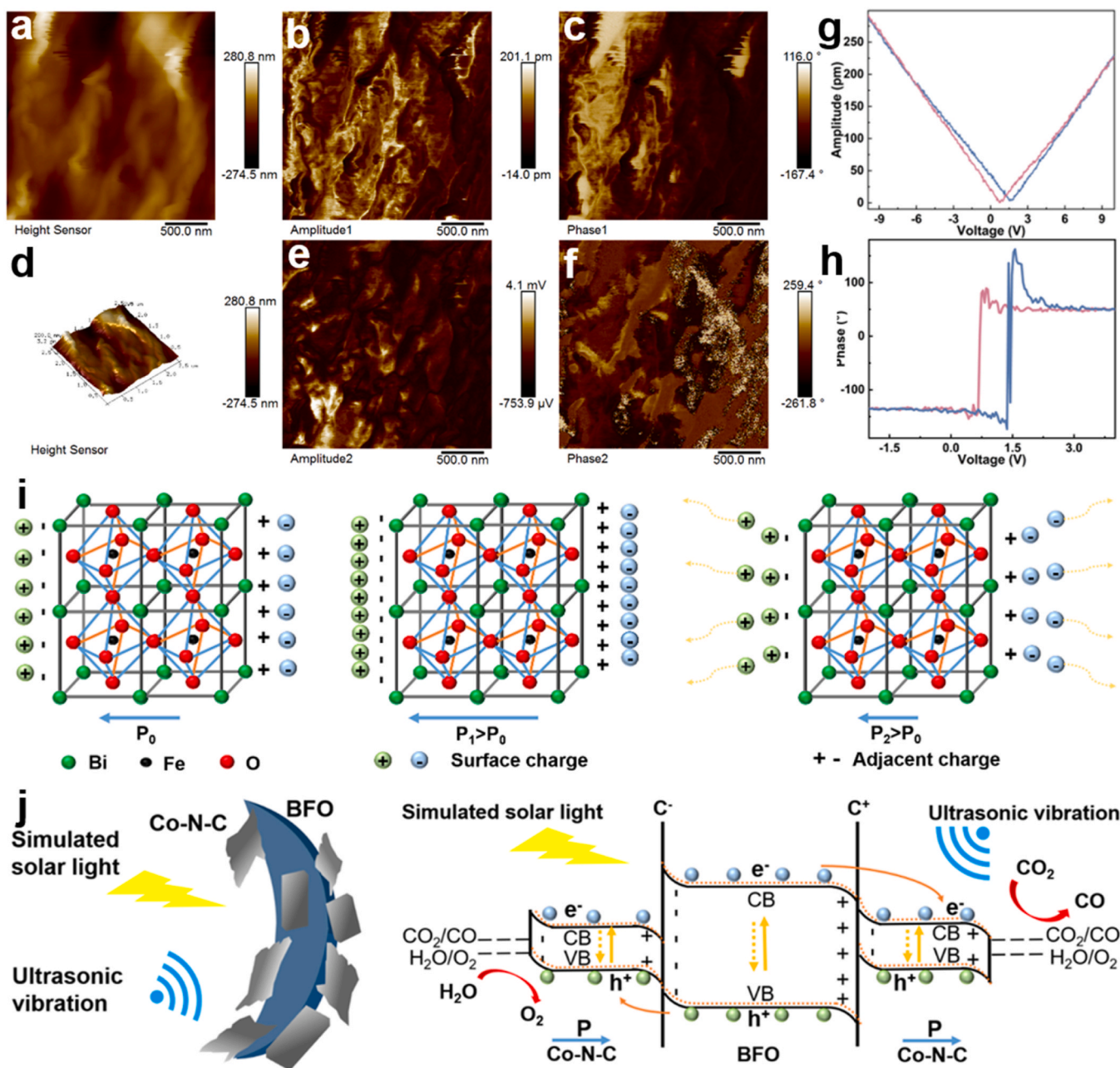
Fig. 4. (a-h) PFM graphics of Co-N-C@BFO. (i) Schematic illustration of charge accumulation and release when spontaneous potential intensity changes with stress variation. (j) Diagrammatic sketch for the piezo-photocatalytic mechanism of the Co-N-C@BFO heterostructures.

piezoelectric effect [49–51]. Piezoelectric catalysis is an efficient catalytic reaction stemming from the piezoelectric effect. The piezoelectric effect generates charges, however, these charges cannot spontaneously participate in catalytic reactions. Fig. 4i shows the schematic diagram of charge accumulation and release when BFO catalyst spontaneous potential intensity varies with stress. BFO catalysts have a spontaneous internal potential that deposits a certain amount of opposite charges on opposite surfaces. When the BFO catalyst is subjected to tensile and compressive stress, the spontaneous potential will increase and decrease, and the amount of charge on the surface will also accumulate and release. These charges still require electric potential to drive. Interestingly, in the process of piezoelectric catalysis, mechanical vibration causes the catalyst to deform under stress, resulting in a displacement current. Displacement current can promote electron transfer to the active center to take part CO_2RR. Displacement current is the condition of generating potential. More importantly, if there had

been no time-varying electrostatic potential, piezoelectric catalysis would not have occurred. The microbubbles generated during mechanical vibration can meet this requirement. The formation and rupture of bubbles can exert a time-varying stress on piezoelectric catalysts. Hence, the production of displacement current is unstable. At the same time, the required catalytic reaction can only be carried out when the corresponding energy band requirements are met. Moreover, the piezoelectric effect generated during the ultrasonic vibration process of the catalyst is crucial. Some piezoelectric materials do not have semiconductor properties, so they mainly rely on the piezoelectric effect. In this study, BFO was selected as the piezoelectric supplier, while Co-N-C was the active site. Its semiconductor properties are not directly related to the piezoelectric effect.

In summary, from the piezoelectric effect to displacement current, we have a comprehensive understanding of the piezoelectric catalysis mechanism. Under mechanical vibration, bubbles will be produced

continuously, and the bursting of bubbles will supply a time-interval stress on the catalyst. According to the principle of displacement current, piezoelectric catalysis makes BFO produce displacement current and generate electrostatic potential that varies with time. The electrostatic potential that changes over time drives the piezoelectric effect to generate an electron flow, which then is transferred through the BFO surface to the Co-N-C surface. Moreover, the Co-N-C@BFO produces more photogenerated carriers under light conditions. The displacement current generated by these carriers through the piezoelectric effect promotes the segregation of electron holes so that more electrons migrate to the active sites to participate in the reaction of CO_2 reduction. Piezoelectric catalytic and mutual coordination, the catalytic efficiency greatly (Fig. 4j). The band structure of Co-N-C@BFO meets the reduction potential of CO_2RR. For the above reasons, the piezo-photocatalytic process has been completed.

3.5. Piezo-photocatalytic CO_2 reduction reaction

We tested and analyzed the CO_2RR performance of the catalysts. The yields of reducing CO_2 to CO and CH_4 under the condition of piezo-photocatalysis continue to increase within 1–5 h (Fig. 5a-f). The yields of CH_4 and CO of BFO were 27.2 and 159.58 μmol/g respectively when

the piezo-photocatalysis was treated for 5 h, as shown in Fig. 5a. According to Fig. 5b, we can see that the CH_4 and CO yields of Co-N-C are 7.87 and 333.96 μmol/g, respectively, when subjected to ultrasonic vibration and light for 5 h, which indicates that the performance of Co-N-C in reducing CO_2 by piezo-photocatalysis is better than that of BFO. In Fig. 5c-f, we analyzed the CO_2 reduction performance of four kinds of Co-N-C@BFO synthesized with distinct proportions of BFO and Co-N-C within 5 h of piezo-photocatalytic treatment. It is easy to observe that the performance of four kinds of Co-N-C@BFO is much better than that of BFO and Co-N-C, especially the performance of Co-N-C@BFO(1:7) piezo-photocatalyst for CO_2 reduction, which is the best. It shows excellent performance when the catalytic time reaches 5 h. The yield of CO_2 reduction to CH_4 and CO through Co-N-C@BFO(1:7) reaches 169.32 and 1373.41 μmol/g, respectively, which is about 8 times the performance of BFO catalysts. The Co-N-C@BFO(1:7) catalyst obtained after the combination of BFO and Co-N-C with a molar ratio of 1:7 has a higher performance in the piezo-photocatalytic reduction of CO_2 than other catalysts (Fig. 5g). In addition, we tested the photocatalytic and piezoelectric catalytic reduction CO_2 performance of Co-N-C@BFO(1:7), BFO, and Co-N-C catalysts under light and mechanical vibration, respectively. When the light time is 1–5 h, Co-N-C@BFO(1:7), BFO, and Co-N-C reduce CO_2 to CH_4 and CO, and their yields are 32.8 and
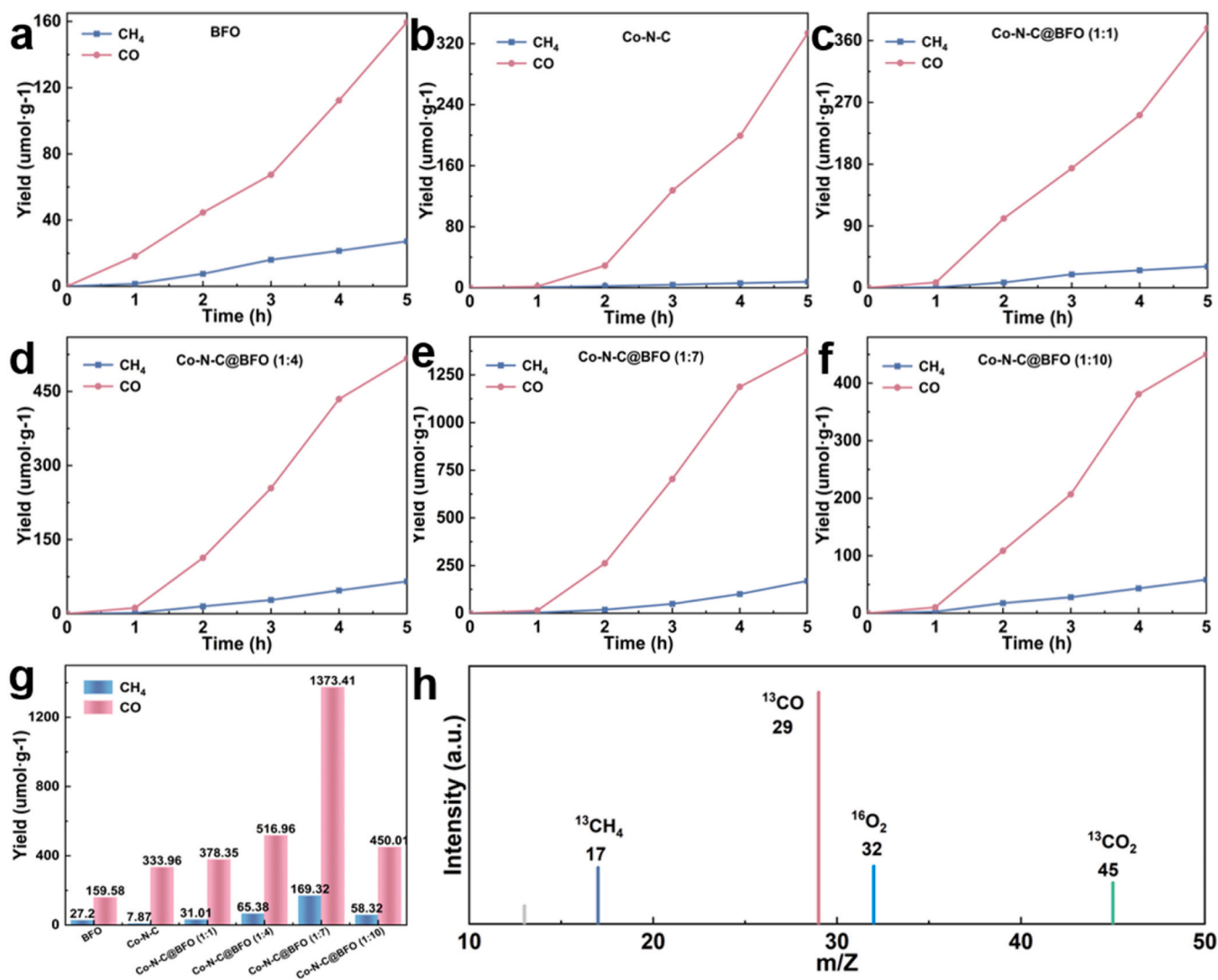

Fig. 5. Trend chart of CO_2 reduction yield of (a) BFO and (b) Co-N-C during 1–5 h of piezo-photocatalysis. Trend chart of CO_2 reduction yield of Co-N-C@BFO (c) 1:1 (d) 1:4 (e) 1:7 and (f) 1:10 during 1–5 h of piezo-photocatalysis. (g) Catalyst comparison of CH_4 and CO reduction yields under 5 h of piezo-photocatalysis. (h) The mass spectra of $^{13}CH_4$ and ^{13}CO generated under a $^{13}CO_2$ atmosphere.

197.07 μmol/g, 6.3 and 61.24 μmol/g, and 6.75 and 94.34 μmol/g, respectively (Fig. S12). After comparison, it is found that the photo-catalytic reduction CO_2 performance of Co-N-C@BFO(1:7) is better than that of BFO and Co-N-C. Based on this, we also tested the performance of piezoelectric catalytic reduction of CO_2. When the mechanical vibration time is 1–5 h, Co-N-C@BFO(1:7), BFO, and Co-N-C reduce CO_2 to CH_4 and CO, with yields of 77.15 and 249.47 μmol/g, 7.4 and 114.8 μmol/g, and 19.03 and 196.01 μmol/g, respectively (Fig. S13). It is further explained that the Co-N-C@BFO(1:7) catalyst has better performance in reducing CO_2 by piezoelectric catalysis. Therefore, we believe that the Co-N-C@BFO obtained by combining BFO and Co-N-C can greatly improve the CO_2 reduction performance. Moreover, the Co-N-C@BFO (1:7), which is compounded by the molar ratio of BFO and Co-N-C being 1:7, has the best catalytic reduction performance for CO_2.

We need to analyze and verify whether CO and CH_4 are obtained from CO_2 reduction during the piezo-photocatalytic reduction of CO_2. So we used isotope labeling of ^{13}CO and $^{13}CH_4$ and used $^{13}CO_2$ as the standard gas for mass spectrometry analysis (Fig. 5h). The experimental results clearly showed peaks of $m/z = 29$ (^{13}CO) and $m/z = 17$ ($^{13}CH_4$). This is sufficient to indicate that CO and CH_4 are products of CO_2 reduction.

3.6. CO_2 reduction mechanism

In-situ DRIFTS were conducted on catalysts to explore the activation and adsorption mechanisms of the CO_2 reduction process (Fig. 6a-i). Generally speaking, CO_2RR involves three processes: adsorption and activation of CO_2, reduction of active CO_2 (production of intermediates), changes in the end product, and desorption [52]. During the above reduction process, different groups will be generated, which are in-termediates for CO_2 reduction. Take the Co-N-C@BFO in Fig. 6g-h as an example. The peak of the surface intermediate at 1334 cm^{-1} was because of the bending vibration of the CO_2* radical under 60 min of continuous light exposure. Interestingly, we can clearly see the pro-duction of CO_2* free radicals, which confirms that the Co-N-C@BFO can adsorb and activate CO_2. In the process of catalytic reduction of CO_2, the COOH* group near 1782 cm^{-1} is also particularly critical. The peaks near 888 and 1110 cm^{-1} are CH_3O* and CHO* intermediates, respec-tively. CHO* intermediates are typically key intermediates for CO_2 reduction. In addition, there are two peaks at 1557 and 2042 cm^{-1}, which belong to the HCO_3* and CO* groups. The growth of CO* intermediates is attributed to the continued protonation of the COOH* group, and the CO* intermediates on Co-N-C@BFO have important reduction steps: i) the rapid protonation of the CO* group, which further generates CHO* intermediates, forming CH_4; ii) the
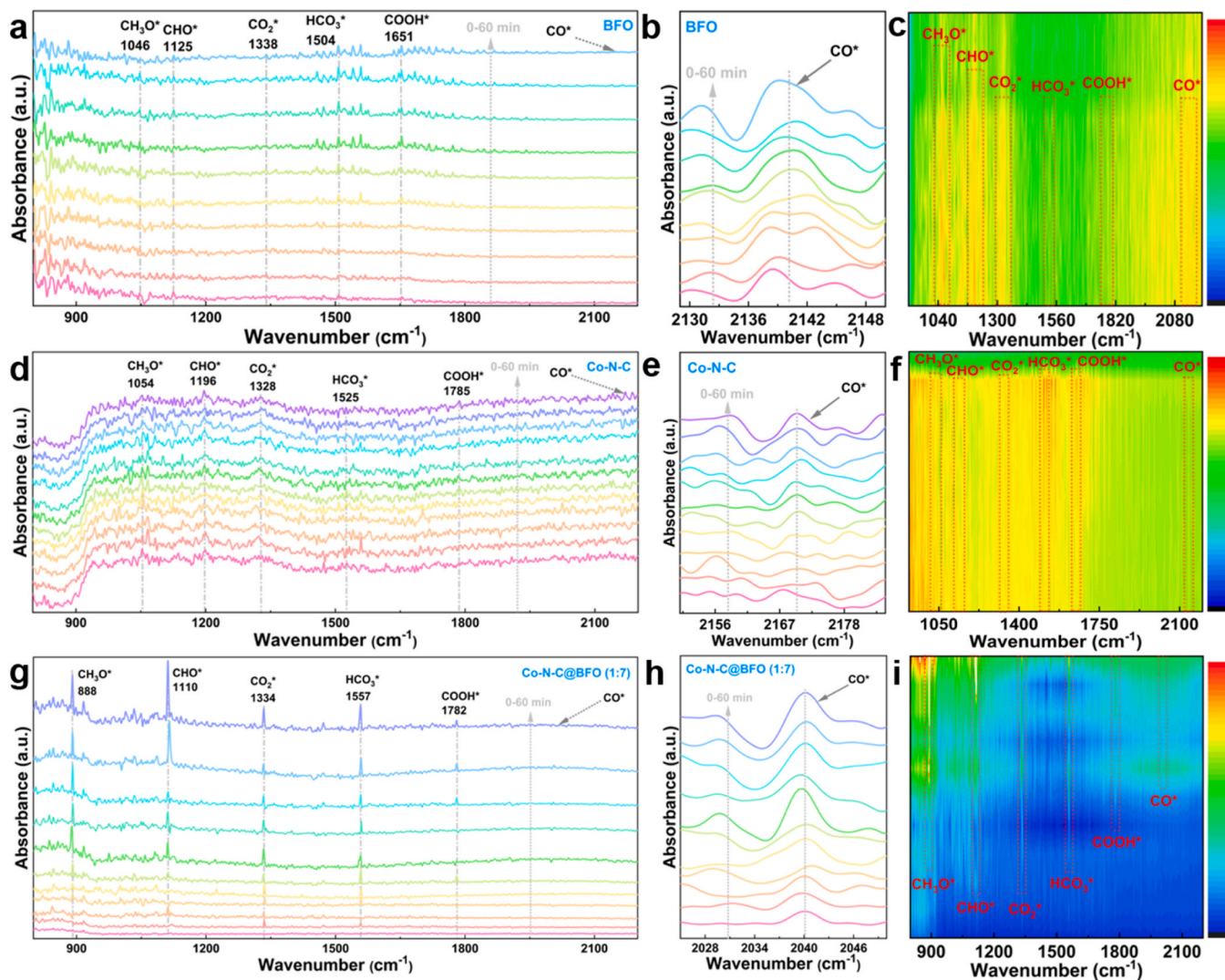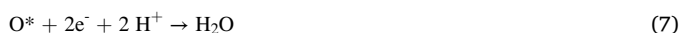

Fig. 6. In-situ DRIFT spectra over (a-b) BFO, (d-e) Co-N-C, and (g-h) Co-N-C@BFO catalysts for visible light driven CO_2 reduction. Contour maps of the in-situ DRIFT of (c) BFO, (f) Co-N-C, and (i) Co-N-C@BFO catalysts.

CO* group does not convert to other intermediates but instead produces CO products [53]. The above species are usually used as intermediates for the CO_2RR. For the Co-N-C@BFO catalyst, these absorption peaks increase with increasing illumination time, indicating the formation of intermediates. The reduction path of CO_2RR on the Co-N-C@BFO catalyst is as follows [54]:

$$CO_2 + e^- + H^+ \rightarrow COOH* \tag{1}$$

$$COOH* + e^- + H^+ \rightarrow CO* + H_2O \tag{2}$$

$$CO* \rightarrow CO\uparrow \tag{3}$$

$$CO* + e^- + H^+ \rightarrow CHO* \tag{4}$$

$$CHO* + 2e^- + 2H^+ \rightarrow CH_3O* \tag{5}$$

$$CH_3O* + e^- + H^+ \rightarrow CH_4\uparrow + O* \tag{6}$$

$$O* + 2e^- + 2H^+ \rightarrow H_2O \tag{7}$$

Furthermore, the peak strength of intermediates increased with increasing light duration, which intuitively confirms that more and more functional groups are generated. The changes of each functional group are clearly visible in the contour maps of the in-situ DRIFT (Fig. 6c, f, i). With the recombination of Co-N-C and BFO, the peaks of HCO_3* and CH_3O* groups produced on the Co-N-C@BFO were enhanced. To sum up, we can know that the Co-N-C@BFO obtained by combining BFO and Co-N-C has a stronger ability to capture photoelectrons. Not only that, but it can also accelerate electron transfer to the adsorbed CO_2 molecules, greatly promoting the production of CHO* intermediates. It also shows that Co-N-C provides more catalytic active sites for Co-N-C@BFO, which can enhance the catalytic reduction activity of CO_2.

4. Conclusion

Therefore, to explore the feasibility and mechanism of piezo-photocatalytic reduction of CO_2, we synthesized Co-N-C@BFO catalyst, and used it in photocatalysis, piezoelectric catalysis and piezo-photocatalytic reduction of CO_2. The results show the CO_2RR performance of the Co-N-C@BFO is higher than that of other catalysts, especially under piezo-photocatalysis. When the duration of ultrasonic vibration and illumination is 5 h, the yields of CO and CH_4 reduced by CO_2 reach 1373.41 and 169.32 μmol/g, respectively. The enhanced performance is due to 1) the introduction of high active Co-N-C, which provides more CO_2RR reaction active sites; 2) the combined action of piezoelectricity and light renders that the charges on BFO are separated rapidly, and electrons are transferred to Co-N-C for the CO_2RR reaction.

CRediT authorship contribution statement

Qijun Xu: Writing - original draft. **Lilian Wang:** Methodology. **Xuelin Sheng**: Modification. **Yongxin Yang:** Data curation. **Conghui Zhang:** Formal analysis. **Lingyan Duan:** Validation. **Hong Guo:** Conceptualization, Supervision, Formal analysis, Writing – original draft, Writing – review & editing, Resources.

Declaration of Competing Interest

The authors declare that they have no known competing financial interests or personal relationships that could have appeared to influence the work reported in this paper.

Data Availability

Data will be made available on request.

Appendix A. Supporting information

Supplementary data associated with this article can be found in the online version at doi:10.1016/j.apcatb.2023.123058.

References

[1] Y.-Y. Xu, S. Li, M. Chen, J.-M. Zhang, F. Rosei, Carbon-based nanostructures for emerging photocatalysis: CO_2 reduction, N_2 fixation, and organic conversion, Trends Chem. 4 (2022) 984–1004.

[2] F. Zhang, Y.-H. Li, M.-Y. Qi, Z.-R. Tang, Y.-J. Xu, Boosting the activity and stability of Ag-Cu_2O/ZnO nanorods for photocatalytic CO_2 reduction, Appl. Catal. B Environ. 268 (2020), 118380.

[3] S.-H. Duan, S.-F. Wu, L. Wang, H.-D. She, J.-W. Huang, Q.-Z. Wang, Rod-shaped metal organic framework structured PCN-222 (Cu)/TiO_2 composites for efficient photocatalytic CO_2 reduction, Acta Phys. Chim. Sin. 36 (2020), 1905086.

[4] Q.-J. Xu, J.-W. Jiang, X.-F. Wang, L.-Y. Duan, H. Guo, Understanding oxygen vacant hollow structure CeO_2@In_2O_3 heterojunction to promote CO_2 reduction, Rare Met 42 (2023) 1888–1898.

[5] Q.-J. Xu, J.-W. Jiang, X.-L. Sheng, Q. Jing, X.-F. Wang, L.-Y. Duan, H. Guo, Understanding the synergistic effect of piezoelectric polarization and extra electrons contributed by oxygen vacancies on efficient piezo-photocatalysis CO_2 reduction, Inorg. Chem. Front. 10 (2023) 2939–2950.

[6] M. Zhang, X.-X. Xuan, W.-L. Wang, C.-Y. Ma, Z.-Q. Lin, Anode photovoltage compensation-enabled synergistic CO_2 photoelectrocatalytic reduction on a flower-like graphene-decorated Cu foam cathode, Adv. Funct. Mater. 30 (2020), 2005983.

[7] W. Zhou, J.-K. Guo, S. Shen, J.-B. Pan, J. Tang, L. Chen, C.-T. Au, S.-F. Yin, Progress in photoelectrocatalytic reduction of carbon dioxide, Acta Phys. Chim. Sin. 36 (2020), 1906048.

[8] B.-W. Deng, H. Song, K. Peng, Q. Li, J.-H. Ye, Metal-organic framework-derived Ga-Cu/CeO_2 catalyst for highly efficient photothermal catalytic CO_2 reduction, Appl. Catal. B Environ. 298 (2021), 120519.

[9] S.-Y. Xu, L.-M. Guo, Q.-J. Sun, Z.-L. Wang, Piezotronic effect enhanced plasmonic photocatalysis by AuNPs/$BaTiO_3$ heterostructures, Adv. Funct. Mater. 29 (2019), 1808737.

[10] J. He, X.-D. Wang, S.-Y. Lan, H.-C. Tao, X.-Z. Luo, Y.-T. Zhou, M.-S. Zhu, Breaking the intrinsic activity barriers of perovskite oxides photocatalysts for catalytic CO_2 reduction via piezoelectric polarization, Appl. Catal. B Environ. 317 (2022), 121747.

[11] L. Persano, A. Camposeo, A.V. Terentjevs, F.D. Sala, E. Fabiano, M. Montinaro, D. Pisignano, Electrostatic mechanophores in tuneable light-emitting piezopolymer nanowires, Adv. Mater. 29 (2017), 1701031.

[12] J. Wu, N. Qin, D.-H. Bao, Effective enhancement of piezocatalytic activity of $BaTiO_3$ nanowires under ultrasonic vibration, Nano Energy 45 (2018) 44–51.

[13] P.-F. Shen, P. Yin, Y.-T. Zou, M. Li, N.-Q. Zhang, D. Tan, H.-Y. Zhao, Q.-J. Li, R.-S. Yang, B. Zou, B.-B. Liu, Ultra-fast piezocatalysts enabled by interfacial onteraction of reduced graphene oxide/MoS_2 heterostructures, Adv. Mater. 35 (2023), 2212172.

[14] Z.-R. Ren, F. Chen, Q. Zhao, G.-Q. Zhao, H. Li, W.-P. Sun, H.-W. Huang, T.-Y. Ma, Efficient CO_2 reduction to reveal the piezocatalytic mechanism: From displacement current to active sites, Appl. Catal. B Environ. 320 (2023), 122007.

[15] X.-F. Zhou, F. Yan, S.-H. Wu, B. Shen, H.-R. Zeng, J.-W. Zhai, Remarkable piezophoto coupling catalysis behavior of BiOX/$BaTiO_3$ (X = Cl, Br, $Cl_{0.166}Br_{0.834}$) piezoelectric composites, Small 16 (2020), 2001573.

[16] W.-F. Io, M.-C. Wong, S.-Y. Pang, Y.-Q. Zhao, R. Ding, F. Guo, J.-H. Hao, Strong piezoelectric response in layered $CuInP_2S_6$ nanosheets for piezoelectric nanogenerators, Nano Energy 99 (2022), 107371.

[17] C.-Y. Jiang, L. Jing, X. Huang, M.-M. Liu, C.-H. Du, T. Liu, X. Pu, W.-G. Hu, Z.-L. Wang, Enhanced solar cell conversion efficiency of inGaN/GaN multiple quantum wells by piezo-phototronic effect, ACS Nano 11 (2017) 9405–9412.

[18] H.-L. You, Z. Wu, L.-H. Zhang, Y.-R. Ying, Y. Liu, L.-F. Fei, X.-X. Chen, Y.-M. Jia, Y.-J. Wang, F.-F. Wang, S. Ju, J.-L. Qiao, C.-H. Lam, H.-T. Huang, Harvesting the vibration energy of $BiFeO_3$ nanosheets for hydrogen evolution, Angew. Chem. Int. Ed. 58 (2019) 11779–11784.

[19] X.-Y. Gao, J.-G. Wu, Y. Yu, Z.-Q. Chu, H.-D. Shi, S.-X. Dong, Giant piezoelectric coefficients in relaxor piezoelectric ceramic PNN-PZT for vibration energy harvesting, Adv. Funct. Mater. 28 (2018), 1706895.

[20] R. Su, H.A. Hsain, M. Wu, D.-W. Zhang, X.-H. Hu, Z.-P. Wang, X.-J. Wang, F.-T. Li, X.-M. Chen, L.-N. Zhu, Y. Yang, Y.-D. Yang, X.-J. Lou, S.J. Pennycook, Nano-ferroelectric for high efficiency overall water splitting under ultrasonic vibration, Angew. Chem. Int. Ed. 58 (2019) 15076–15081.

[21] S.-W. Xu, W.-Q. Qian, D. Zhang, X. Zhao, X.-M. Zhang, C.-B. Li, C.R. Bowen, Y. Yang, A coupled photo-piezo-catalytic effect in a BST-PDMS porous foam for enhanced dye wastewater degradation, Nano Energy 77 (2020), 105305.

[22] W.-D. Ma, J.-F. Lu, B.-S. Wan, D.-F. Peng, Q. Xu, G.-F. Hu, Y.-Y. Peng, C.-F. Pan, Z.-L. Wang, Piezoelectricity in multilayer black phosphorus for piezotronics and nanogenerators, Adv. Mater. 32 (2020), 1905795.

[23] K. Peng, J.-Y. Ye, H.-J. Wang, H. Song, B.-W. Deng, S. Song, Y.-H. Wang, L.-J. Zuo, J.-H. Ye, Natural halloysite nanotubes supported Ru as highly active catalyst for photothermal catalytic CO₂ reduction, Appl. Catal. B Environ. 324 (2023), 122262.

[24] A. Toprak, O. Tigli, Piezoelectric energy harvesting: state-of-the-art and challenges, Appl. Phys. Rev. 1 (2014), 031104.

[25] D.B. Kim, K.S. Jo, K.S. Park, Y.S. Cho, Anion-dependent polarization and piezoelectric power generation in hybrid halide MAPbX₃ (X = I, Br, and Cl) thin films with out-of-plane structural adjustments, Adv. Sci. 10 (2023), 2204462.

[26] Y.-L. Jia, K. Zhang, Piezoelectric potential-enhanced output and nonlinear response range for self-powered sensor on curved surface, Nano Energy 96 (2022), 107103.

[27] Y. Cho, P. Giraud, B. Hou, Y.W. Lee, J. Hong, S. Lee, S. Pak, J. Lee, J.E. Jang, S.M. Morris, J.I. Sohn, S. Cha, J.M. Kim, Charge transport modulation of a flexible quantum dot solar cell using a piezoelectric effect, Adv. Energy Mater. 8 (2018), 1700809.

[28] A. Zhang, Z.-Y. Liu, B. Xie, J.-S. Lu, K. Guo, S.-M. Ke, L.-L. Shu, H.-Q. Fan, Vibration catalysis of eco-friendly Na₀.₅K₀.₅NbO₃-based piezoelectric: an efficient phase boundary catalyst, Appl. Catal. B Environ. 279 (2020), 119353.

[29] C. Stenner, L.H. Shao, N. Mameka, J. Weissmüller, Piezoelectric gold: strong charge-load response in a metal-based hybrid nanomaterial, Adv. Funct. Mater. 26 (2016) 5174–5181.

[30] Y.-Z. Zhang, L.-Y. Yang, Y.-J. Zhang, Z.-Y. Ding, M.-J. Wu, Y. Zhou, C.-L. Diao, H.-W. Zheng, X.-F. Wang, Z.-L. Wang, Enhanced photovoltaic performances of La-doped bismuth ferrite/zinc oxide heterojunction by coupling piezo-phototronic effect and ferroelectricity, ACS Nano 14 (2020) 10723–10732.

[31] Z.-L. Wang, On Maxwell's displacement current for energy and sensors: the origin of nanogenerators, Mater. Today 20 (2017) 74–82.

[32] J.-P. Ma, X. Xiong, D. Wu, Y. Wang, C.-G. Ban, Y.-J. Feng, J.-Z. Meng, X.-S. Gao, J.-Y. Dai, G. Han, L.-Y. Gan, X.-Y. Zhou, Band position-independent piezo-electrocatalysis for ultrahigh CO₂ conversion, Adv. Mater. (2023), 2300027.

[33] K. Shimizu, H. Hojo, Y. Ikuhara, M. Azuma, Enhanced piezoelectric response due to polarization rotation in cobalt-substituted BiFeO₃ epitaxial thin films, Adv. Mater. 28 (2016) 8639–8644.

[34] O. Paull, C.-S. Xu, X. Cheng, Y.-Y. Zhang, B. Xu, K.P. Kelley, A.D. Marco, R.K. Vasudevan, L. Bellaiche, V. Nagarajan, D. Sando, Anisotropic epitaxial stabilization of a low-symmetry ferroelectric with enhanced electromechanical response, Nat. Mater. 21 (2022) 74–80.

[35] L. Liu, T. Rojac, D. Damjanovic, M.D. Michiel, J. Daniels, Frequency-dependent decoupling of domain-wall motion and lattice strain in bismuth ferrite, Nat. Commun. 9 (2018) 4928.

[36] J.-X. Zhang, B. Xiang, Q. He, J. Seidel, R.J. Zeches, P. Yu, S.-Y. Yang, C.-H. Wang, Y.-H. Chu, L.W. Martin, A.M. Minor, R. Ramesh, Large field-induced strains in a lead-free piezoelectric material, Nat. Nanotechnol. 6 (2011) 98–102.

[37] D. Sando, Y.-R. Yang, E. Bousquet, C. Carrétéro, V. Garcia, S. Fusil, D. Dolfi, A. Barthélémy, P. Ghosez, L. Bellaiche, M. Bibes, Large elasto-optic effect and reversible electrochromism in multiferroic BiFeO₃, Nat. Commun. 7 (2016) 10718.

[38] H. Luo, W.-J. Jiang, S. Niu, X. Zhang, Y. Zhang, L.-P. Yuan, C.-X. He, J.-S. Hu, Self-catalyzed growth of Co-N-C nanobrushes for efficient rechargeable Zn-Air batteries, Small 16 (2020), 2001171.

[39] P. Yu, L. Wang, F.-F. Sun, Y. Xie, X. Liu, J.-Y. Ma, X.-W. Wang, C.-G. Tian, J.-H. Li, H.-G. Fu, Co nanoislands rooted on Co-N-C nanosheets as efficient oxygen electrocatalyst for Zn-Air batteries, Adv. Mater. 31 (2019), 1901666.

[40] W. Liu, C. Zhang, J.-J. Zhang, X. Huang, M. Song, J.-W. Li, F. He, H.-P. Yang, J. Zhang, D.-L. Wang, Tuning the atomic configuration of Co-N-C electrocatalyst enables highly-selective H₂O₂ production in acidic media, Appl. Catal. B Environ. 310 (2022), 121312.

[41] Y.-F. Wang, Y.-M. Xu, S.-S. Dong, P. Wang, W. Chen, Z.-D. Lu, D.-J. Ye, B.-C. Pan, D. Wu, C.D. Vecitis, G.-D. Gao, Ultrasonic activation of inert poly (tetrafluoroethylene) enables piezocatalytic generation of reactive oxygen species, Nat. Commun. 12 (2021) 3508.

[42] R. Jamshidi, B. Pohl, U.A. Peuker, G. Brenner, Numerical investigation of sonochemical reactors considering the effect of inhomogeneous bubble clouds on ultrasonic wave propagation, Chem. Eng. J. 189–190 (2012) 364–375.

[43] Y.-Y. Liu, P. Zhao, Y. Liang, Y.-Y. Chen, J.-Z. Pu, J.-Q. Wu, Y.-L. Yang, Y. Ma, Z. Huang, H.-B. Luo, C.-J. Huo, C.-J. Hou, Single-atom nanozymes Co-N-C as an electrochemical sensor for detection of bioactive molecules, Talanta 254 (2023), 124171.

[44] B. Zhang, R. Dugas, G. Rousse, P. Rozier, A.M. Abakumov, J.M. Tarascon, Insertion compounds and composites made by ball milling for advanced sodium-ion batteries, Nat. Commun. 7 (2016) 10308.

[45] D. Liu, P. Yang, H. Zhang, M.-J. Liu, W.-F. Zhang, D.-M. Xu, J. Gao, Direct reductive coupling of nitroarenes and alcohols catalysed by Co-N-C/CNT@AC, Green. Chem. 21 (2019) 2129.

[46] M.-H. Li, S.-Y. Chen, Q.-K. Jiang, Q.-L. Chen, X. Wang, Y. Yan, J. Liu, C.-C. Lv, W.-P. Ding, X.-F. Guo, Origin of the activity of Co-N-C catalysts for chemoselective hydrogenation of nitroarenes, ACS Catal. 11 (5) (2021) 3026–3039.

[47] W. Liu, P.-F. Wang, Y.-H. Ao, J. Chen, X. Gao, B.-H. Jia, T.-Y. Ma, Directing charge transfer in a chemical-bonded BaTiO₃@ReS₂ schottky heterojunction for piezoelectric enhanced photocatalysis, Adv. Mater. 34 (2022), 2202508.

[48] C. Liu, G.-J. Xiao, M.-L. Yang, B. Zou, Z.-L. Zhang, D.-W. Pang, Mechanofluorochromic carbon nanodots: controllable pressuretriggered blue- and red-shifted photoluminescence, Angew. Chem. Int. Ed. 57 (2018) 1893–1897.

[49] E.-Z. Lin, Z.-H. Kang, J. Wu, R. Huang, N. Qin, D.-H. Bao, BaTiO₃ nanocubes/ cuboids with selectively deposited Ag nanoparticles: Efficient piezocatalytic degradation and mechanism, Appl. Catal. B Environ. 285 (2021), 119823.

[50] Q.-Q. Lei, H.-Q. Yuan, J.-H. Du, M. Ming, S. Yang, Y. Chen, J.-X. Lei, Z.-J. Han, Photocatalytic CO₂ reduction with aminoanthraquinone organic dyes, Nat. Commun. 14 (2023) 1087.

[51] C.-Y. Wang, C. Hu, F. Chen, H.-T. Li, Y.-H. Zhang, T.-Y. Ma, H.-W. Huang, Polar layered bismuth-rich oxyhalide piezoelectrics Bi₄O₅X₂ (X=Br, I): Efficient piezocatalytic pure water splitting and interlayer anion-dependent activity, Adv. Funct. Mater. (2023), 2301144.

[52] J.-W. Jiang, X.-F. Wang, Q.-J. Xu, Z.-Y. Mei, L.-Y. Duan, H. Guo, Understanding dual-vacancy heterojunction for boosting photocatalytic CO₂ reduction with highly selective conversion to CH₄, Appl. Catal. B Environ. 316 (2022), 121679.

[53] L.-J. Chen, T.-T. Liu, S.-M. Liu, S. Cai, X.-X. Zou, J.-W. Jiang, Z.-Y. Mei, G.-F. Zhao, X.-F. Yang, H. Guo, S vacant CuIn₅S₈ confined in a few-layer MoSe₂ with interlayerexpanded hollow heterostructures boost photocatalytic CO₂ reduction, Rare Metals 41 (2022) 144–154.

[54] X. Liu, J. Xiao, H. Peng, X. Hong, K. Chan, J.K. Nørskov, Understanding trends in electrochemical carbon dioxide reduction rates, Nat. Commun. 8 (2017) 15438.